Hybrid Amino Acid-TiO$_2$ Materials with Tuneable Crystalline Structure and Morphology for Photocatalytic Applications

Gamze Sarigul, Ignacio Chamorro-Mena, Noemi Linares, Javier García-Martínez,* and Elena Serrano*

A method to produce hybrid organotitanias, both as thin films and suspensions, showing excellent photocatalyic activity in the degradation of organic dyes in aqueous solutions under visible light irradiation is disclosed. This method is based on the in situ incorporation of an amino acid, L-tyrosine, during the synthesis of the titanias owing to its coordination and co-condensation with the titania precursor under acidic conditions. This methodology allows the fine-tuning of their crystalline structure, size, and shape by simply varying the pH of the synthesis gel, leading to anatase nanoparticles of ≈5 nm and surface areas of ≈200 m^2 g^{-1} at pH = 2.2, while highly crystalline rutile nanorods are formed at pH = 0. The incorporation of L-tyrosine to both anatase nanoparticles and rutile nanorods enables these materials to absorb light in the visible range due to both the decrease in their band gap, as compared to the reference materials, and the presence of additional absorption edges at wavelengths higher than 400 nm. Consequently, the photocatalytic activity of both hybrid anatase nanoparticles and rutile nanorods exhibits a 120% enhanced photocatalytic efficiency, as compared to that of L-Tyr-free titanias and the commercial P25, which confirms their potential application in water remediation.

1. Introduction

Photocatalysis offers the unique possibility of producing chemicals and/or degrade pollutants using a sustainable and renewable source of energy, namely sunlight. To achieve this goal, the photoactive materials should be designed and optimized to improve their efficiency under visible light.[1] The most used photocatalyst,

titanium dioxide in its anatase (A) phase, TiO$_2$ (A), presents remarkable properties under UV light, which are very useful in photo-oxidation reactions. Some of these are, its chemical stability, low cost, availability, and low toxicity.[2] However, as it is widely known, it presents limited photoactivity under visible light. We have recently described a novel strategy, based on the in situ incorporation of organic moieties or metallic complexes during the synthesis of titania, which drastically enhances its photocatalytic efficiency under sunlight irradiation.[3–6]

By using this strategy, a series of visible light-activated hybrid anatase nanoparticles have been produced by the in situ incorporation of organic compounds such as p-phenylenediamime, as well as Ru(II) or Ir(III) complexes, among others, to titania, using water and ethanol as solvents.[3–5] This methodology yields materials with a reduced band gap, absorption edges in the visible light, and outstanding stability; all of these features synergistically contributing to enhancing their photoactivity.[3–6] Furthermore, the integration of our hybrid titania containing the Ru(II) N3 dye into a photoelectrode of a low-temperature dye-sensitized solar cells (lt-DSSC) yielded the highest efficiency reported to date for titania-based lt-DSSCs (8.75%).[7] Very recently, we have reported the first biphasic rutile-brookite organotitania nanoparticles synthesized under mild conditions using 1,10-phenanthroline as both crystal modifier and as a source of intermediate N2p levels. Owing to these features, the hybrid organotitanias exhibit outstanding photocatalytic activity under visible light irradiation.[6] In light of these results, we decided to extend our approach to other morphologies and synthetic conditions, by incorporating other organic compounds. In this contribution, we report the synthesis, characterization, and catalytic testing of a series of hybrid amino acid-titania anatase nanoparticles and rutile nanorods with enhanced photocatalytic activity under visible light irradiation.

Amino acids can be effectively incorporated in titania by coordinating their amine and carboxylic groups to the titanium atom of the titania precursor.[8,9] In fact, different amino acids have been used as shape-modifiers in the synthesis of brookite and rutile titanias, prepared with titanium metal powder and ammonia solutions.[8] The photodeposition of Pt co-catalyst on the surface of the as-synthesized brookite particles led

G. Sarigul, I. Chamorro-Mena, Dr. N. Linares, Prof. J. García-Martínez, Dr. E. Serrano
Universidad de Alicante
Departamento de Química Inorgánica
Laboratorio de Nanotecnología Molecular
Ctra. San Vicente-Alicante s/n
Alicante E-03690, Spain
E-mail: j.garcia@ua.es; elena.serrano@ua.es

The ORCID identification number(s) for the author(s) of this article can be found under https://doi.org/10.1002/adsu.202100076.

**ADVANCED
SCIENCE NEWS**
www.advancedsciencenews.com
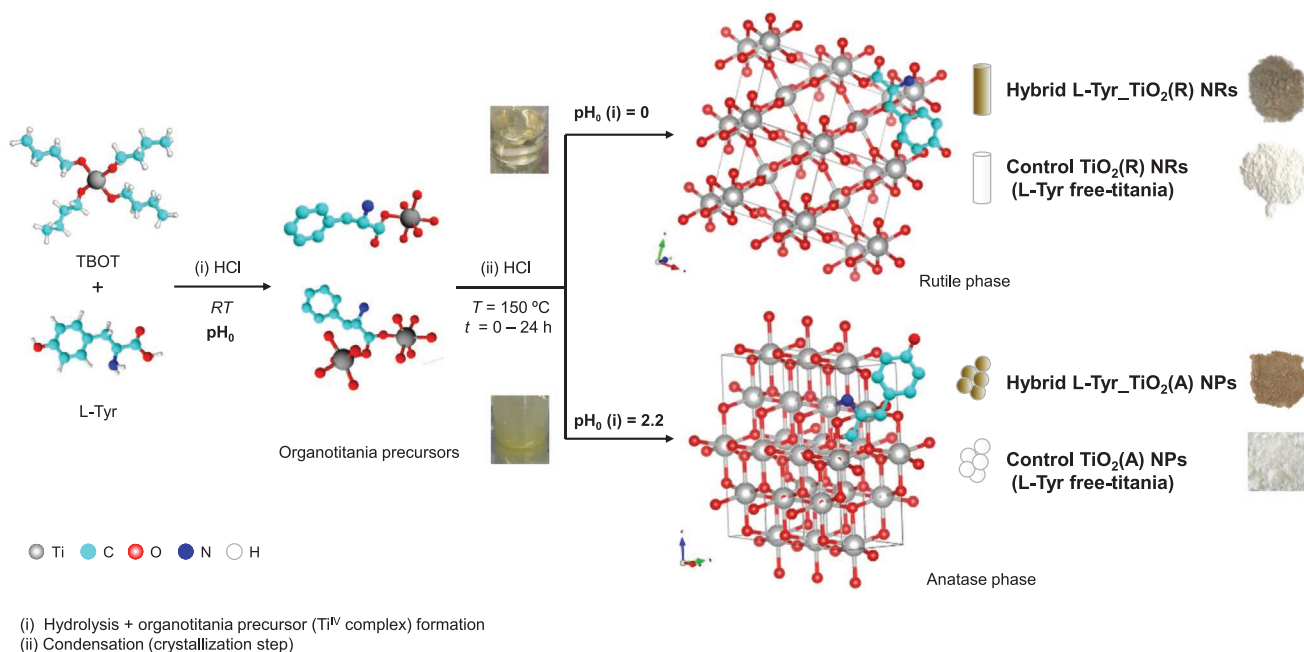
**ADVANCED
SUSTAINABLE
SYSTEMS**
www.advsustainsys.com

to an enhanced photocatalytic CO_2 reduction under UV–vis irradiation.[8] On the other hand, the formation of titanium dioxide particles from a $TiCl_4$ precursor in the presence of various amino acids led to different phase distributions (brookite and/or anatase), sizes, and shapes of the formed nanoparticles, depending on the amino acid used.[10] The authors concluded that each amino acid binds preferentially to one specific face, for example, Glu to the {101} surface of anatase while His to the {001} one. Thus, the growth of TiO_2 in the presence of amino acids may allow, not only for the preferential growth of a certain polymorph, but also of an exposed face, which is particularly interesting for photocatalysis and solar cells applications.[10] In a similar process, but using chemical bath deposition for the formation of films,[11] the use of amino acids in the deposition solution allowed for the fine control of the thickness and roughness of the films. The synthesis of all these materials was performed under acidic-neutral conditions; however, similar results were obtained in basic conditions, under which the use of a basic amino acid, such as arginine, enabled the self-assembly of the TiO_2 nuclei which resulted in the formation of bean-like anisotropic titania nanoparticles.[12]

While the effect of amino acids (including L-Tyr) as capping agents in the structural and physico-chemical properties of titania materials has been previously evaluated, their use as photocatalyts has been scarcely studied.[13,14] Herein, we report the preparation of hybrid amino acid-titania rutile nanorods and anatase nanoparticles as a proof of concept of novel amino acid-modified semiconductors, through the reaction of the titania precursor with L-tyrosine (L-Tyr) prior to the hydrolysis and condensation of the alkoxy titanate. L-Tyr has been chosen because of i) its solubility at extreme pH, and ii) the fact that the L-Tyr addition to the synthesis gel does not affect the pH
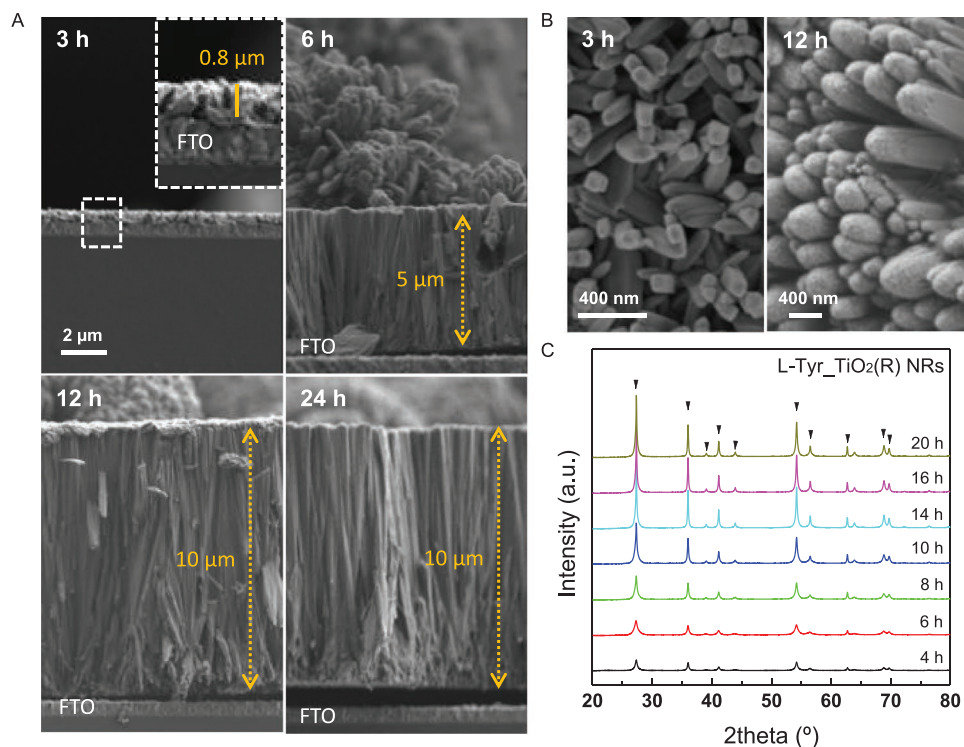
of the solutions under the tested conditions, as previously reported for this amino acid.[8] The incorporation of L-Tyr up to 1 wt% does not compromise the main structural and physico-chemical properties of the final materials. The control of their morphology and structure was achieved by tuning the pH of the synthetic mixture. The hybrid materials exhibit optimized optical properties, which yield a twofold enhancement of their photocatalytic activity, as compared to the non-modified control titanias and the commercial P25.

2. Results and Discussion

Hybrid L-Tyr_TiO_2 organotitanias were synthesized under acidic hydrothermal conditions, using tetrabutyl orthotitanate (TBOT) as titania precursor and L-Tyr—**Scheme 1**. First, the titania precursor and the L-Tyr were directly mixed at room temperature (RT) and, subsequently, HCl was added to adjust the pH of the synthetic mixture at pH = 0 or 2.20—Scheme 1,i. As previously reported for non-modified titanias,[15] the hydrolysis of the TBOT is completed at RT even under highly acidic conditions, leading to the substitution of the OR^- ligands in TBOT by strongly nucleophilic hydroxo groups (OH^-), which are generated from the dissociation of water. Under these conditions, the Ti(IV) forms positively charged octahedral complexes, $[Ti(OH)_{4-n}(OH_2)_{2+n}]^{n+}$, $n = 1,2,3$, delaying their immediate condensation. The direct reaction of TBOT with L-Tyr at pH = 0 leads to a yellow clear solution, while the increase of the pH up to 2.2 causes a yellowish suspension at RT—Scheme 1,ii (optical images). This could be explained by taking into account that the degree of protonation of those Ti(IV) octahedral complexes decreases with acidity, shifting the hydrolysis equilibrium to the

(i) Hydrolysis + organotitania precursor (Ti^{IV} complex) formation
(ii) Condensation (crystallization step)

Scheme 1. Schematic illustration of the synthesis of the hybrid L-Tyr_TiO_2 (R) NRs and L-Tyr_TiO_2 (A) NPs, starting from the titania precursor TBOT and L-tyrosine (L-Tyr), and the proposed structure. Control TiO_2 (L-Tyr free-titania) NRs, TiO_2(R), and NPs, TiO_2(A), were synthesized using the same conditions.

**ADVANCED
SCIENCE NEWS**

www.advancedsciencenews.com

**ADVANCED
SUSTAINABLE
SYSTEMS**

www.advsustainsys.com

Figure 1. A) Cross-sectional (same scale) and B) top view (same scale) FESEM images, as well as C) X-ray synchrotron patterns of the FTO-based hybrid L-Tyr_TiO$_2$(R) NRs films at different crystallization times at 150 °C. Arrows in (C) indicate the peaks corresponding to the rutile phase.

formation of neutral complexes that could aggregate to form amorphous titania.[15–17] The yellow color of the initial solutions/suspensions suggests the formation of some intermediates due to the TBOT reaction with L-Tyr. Based on the pK_a values of the phenolic hydroxyl (10.22), amino (9.11), and carboxylate (2.20) groups in L-Tyr, and the strong acidic conditions used, those intermediates are proposed to be mainly formed by dititanium units through bidentate bridging carboxylic groups (carboxylate groups at pH = 2.2) or even to monodentate coordination to titanium centers, as previously described elsewhere for similar bonding situations—Scheme 1,i.[3,9,18,19]

In a second step, those titanium-tyrosine complexes were used as organotitania precursors for the synthesis of the hybrid L-Tyr_TiO$_2$ samples. They were crystallized at 150 °C in a Teflon lined stainless steel autoclave, where a fluorine-doped tin oxide (FTO) glass was also introduced—Scheme 1,ii. After filtering the suspensions and washing both the FTO-films and the suspensions, gray/brown colored materials were obtained in all cases. At pH = 2, the FTO did not contain much titania, in line with the initial yellowish suspension observed at RT for this sample. The incorporation of L-Tyr in the final materials was ≈1 wt%, as determined by thermogravimetric (TG) measurements—Figure S1, Supporting Information. For comparison purposes, L-Tyr-free control titanias were produced following the same experimental procedure, being in all cases white solids.

The morphology and structural analysis of the as-synthesized materials were examined by synchrotron X-ray diffraction, field emission scanning electron microscopy (FESEM), and transmission electron microscopy (TEM)—**Figures 1** and **2**. As

described below, the addition of L-Tyrosine during the synthesis of the titania does not entail any change in the morphology or size, indicating that the pH directs the phase and morphology of the final solids, even with the incorporation of the amino acid to the synthesis. The hybrid L-Tyr_TiO$_2$(R) NRs present strong diffraction peaks that can be indexed to the tetragonal structure of rutile (JCPDS 21-1276), whose intensity increases till ≈14 h of crystallization at 150 °C—Figures 1C and 2C. As compared to the control titania, the crystallization of rutile is only slightly delayed at low crystallization times, probably due to the low L-Tyr amount incorporated—Figure S2, Supporting Information. The particle size calculated by applying the Scherrer equation to the deconvoluted main peak of rutile at $2\theta = 27.4°$ also increases with the crystallization time, reaching a plateau after ≈14 h of treatment in the range of 35–45 nm. The X-ray diffraction patterns were fitted by 50–50% Lorentzian–Gaussian curves. The results discard the presence of both anatase and brookite phases—see Figure S3, Supporting Information and ESI for further details. The presence of the characteristic peaks of the rutile structure, as well as the match of their relative intensities with the standard of rutile at the different crystallization times, is in agreement with the polycrystalline nature of these samples, as previously observed for similar materials[20] and confirmed by selected area electron diffraction (SAED) analysis (vide infra). It should be noted that no differences have been found in the X-ray diffraction patterns and morphology of both FTO-based films and powder suspensions recovered from the autoclave—Figure S4, Supporting Information.

Cross-sectional FESEM images of the FTO-films reveal a first layer of rutile nanorod bundles.[15,21,22] Each nanorod
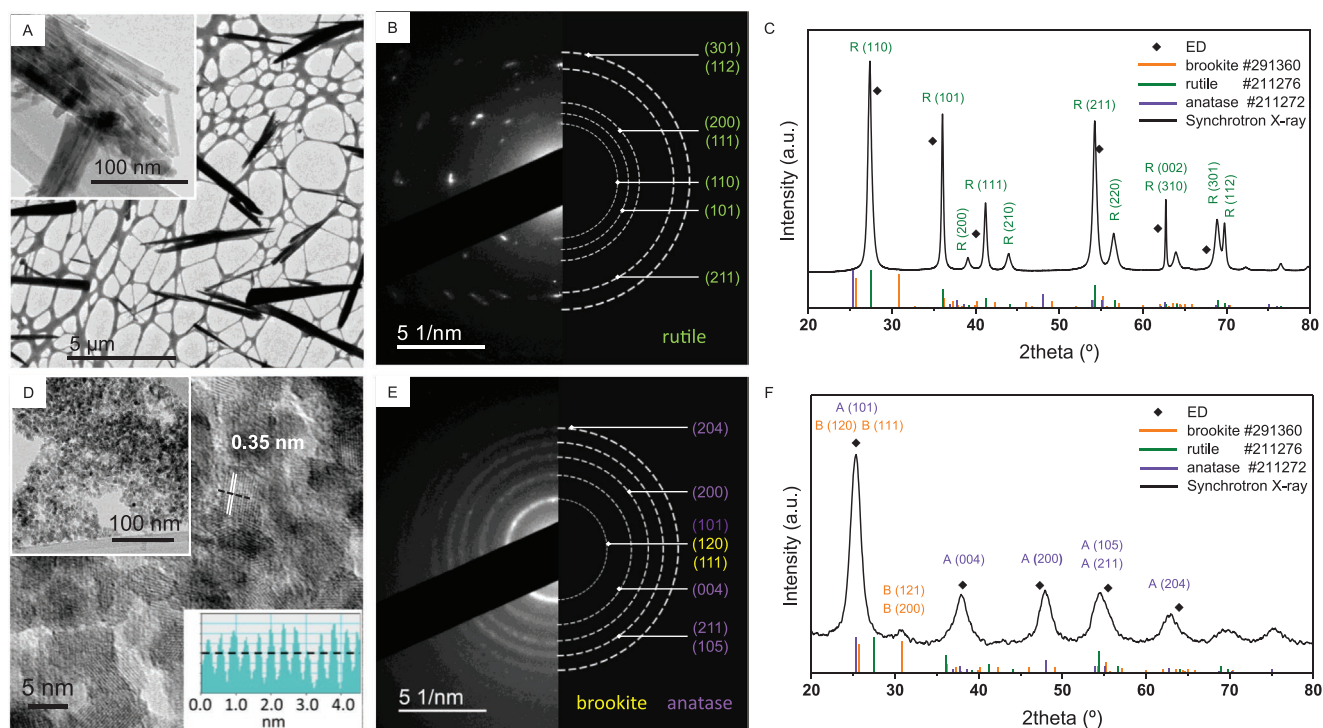
Figure 2. A) Morphology and structural analysis of the hybrid L-Tyr_TiO₂(R) NRs (top) and L-Tyr_TiO₂ NPs (bottom) after 24 h of crystallization at 150 °C: A,D) TEM micrographs at two different magnifications, B,E) selected area electron diffraction (SAED) patterns of a TEM image at low magnification, and C) synchrotron and F) conventional XRD patterns showing the 2θ data calculated from the SAED analysis. XRD patterns of the standard PDF cards of anatase, rutile, and brookite are included in (C) and (F) for comparison purposes.

is ≈0.8 mm length and 90 nm diameter after 3 h of thermal treatment at 150 °C. As the crystallization time increases, two phenomena are observed. On one hand, the first layer quickly increases in height until reaching a constant value of ≈10 µm after 12 h of crystallization. This is consistent with the observed changes in the intensity of the diffraction peaks—Figure 1A. And on the other hand, additional growing of rutile bundles on the top of the first layer was observed after 4 h of crystallization in the case of hybrid titanias, leading to well-interconnected crystallites of ≈500 nm in diameter—see also Figure S5, Supporting Information.[20]

Similar morphologies have been previously obtained for non-modified titanias synthesized by acid-assisted hydrothermal method, which have been defined as multilevel branched rutile or titania nanoflowers.[15,23] Indeed, TEM analysis confirmed the formation of rutile fibers (≈10 nm of diameter) and bundles roughly aligned along the crystallographic c–axis—Figure 2A.

It is well known that the transformation of anatase to rutile is promoted by strong acidity, as rutile is the favorable phase at very low pH.[21,24–26] Accordingly, when the synthesis was carried out at pH = 2.2 instead of pH = 0 by reducing the HCl concentration—Scheme 1, bottom part—anatase-brookite (≈10% brookite) nanoparticles were obtained. An average particle size of ≈5.3 nm (7.0 nm for brookite) was determined by applying the Scherrer equation to the deconvoluted main peaks of anatase at 2θ = 25.5° (101) and brookite at 2θ = 31.0°—Figure 2F and Figure S6, Supporting Information. Because the main peak of anatase phase at ≈2θ = 25.5° (101) coincides with two of the most intense peaks of brookite at 2θ = 25.5° (120)

and 25.9° (111), both the brookite content and its particle size were obtained by careful deconvolution of the experimental data, as described elsewhere (see ESI for details).[6,27,28] TEM analysis of L-Tyr_TiO₂(A) NPs confirms the anatase structure of the materials obtained. The lattice fringes with an interplanar spacing of ≈0.35 nm coincide with the planar distance in the (101) orientation of anatase—Figure 2D. The SAED patterns of the low magnification TEM images of both hybrid NRs and NPs—Figure 2B,E, respectively—exhibit a set of bright rings, which are characteristic of polycrystalline materials—see also Figures S7 and S8, Supporting Information. The 2θ values calculated from the SAED analysis, the X-ray synchrotron data, and the standard PDF cards allowed us to identify the specific diffractions of rutile—Figure 2C—and anatase—Figure 2F.

The surface characterization of as-synthesized materials was carried out by X-ray photoelectron spectroscopy (XPS)—Figure S9, Supporting Information. XPS spectra in the Ti2p region of the control and the hybrid NPs and NRs feature 2p³/² and 2p¹/² peaks at ≈458.4 and 464 eV, with a spin orbit splitting in the range of 5.70–5.75 eV. A blue-shift of 0.13 eV and 0.15 eV, is observed for the hybrid NPs and the NRs, respectively, as compared to the control (L-Tyr-free) titanias. The peak positions and orbit splitting agrees well with the binding energy reported for Ti(IV) in anatase and rutile titanias and organotitanias.[4,6,29,30] These bands do not show additional lower binding energy components associated with the presence of reduced Ti³⁺ centers. XPS spectra in the O1s region were also fitted to determine the binding states of oxygen in both hybrid and control NPs and NRs—Figure S10C,D, Supporting Information. The main peak

Adv. Sustainable Syst. **2021**, *5*, 2100076

2100076 (4 of 11)

2021 The Authors. Advanced Sustainable Systems published by Wiley-VCH GmbH

**ADVANCED
SCIENCE NEWS**
www.advancedsciencenews.com

**ADVANCED
SUSTAINABLE
SYSTEMS**
www.advsustainsys.com

Table 1. Optical band gap, BET areas, and constant values of the photocatalytic activity under VIS irradiation, regression coefficients, and conversions at different times of the hybrids L-Tyr_TiO$_2$(R) NRs and L-Tyr_TiO$_2$(A) NPs (crystallization time 24 h) as compared with the control experiments. Experiments were carried out under identical irradiation conditions, using 40 mg of photocatalyst and 100 mL of 1×10^{-5} M aqueous Rh6G solutions.

| Sample	E_g [eV]			S_{BET}[d] [m^2 g^{-1}]	$k' \times 10^{3}$ [e] [min^{-1}]	R^{2} [f]	[g]Conversion		k'/k'_{P25}[h]
	[a]Abs.	[b]Direct	[c]Indirect				20 min	200 min	
L-Tyr_TiO$_2$(R) NRs	2.88	2.9	2.7	30	3.85 ± 0.07 (3.9)	0.9972	15	47	2.2 ± 0.4
L-Tyr_TiO$_2$(A) NPs	2.92	3.0	2.5	205	3.95 ± 0.64 (3.95)	0.9933	14	48	2.2 ± 0.7
TiO$_2$(R) NRs	2.98	3.0	2.9	20	2.35 ± 0.07 (2.3)	0.9981	9	36	1.3 ± 0.3
TiO$_2$(A) NPs	3.14	3.2	3.0	200	1.91 ± 0.21 (1.7)	0.9782	5	29	1.1 ± 0.3
P25	—	3.5	3.4	65	1.76 ± 0.29 (1.6)	0.9872	6	27	—

[a]Band gap estimation directly read from the diffuse reflectance spectra energies, and; [b]calculated from the intercept of the tangent to the $(F(R)h\nu)^2$ versus $(h\nu)$ plot (direct band gap) or; [c]the $(F(R)h\nu)^{1/2}$ versus $(h\nu)$ plot (indirect band gap); [d]BET surface area (S_{BET}) from N$_2$ adsorption/desorption isotherms at 77 K; [e]Pseudo-first order rate constant (k') and; [f]regression coefficient (R^2) of the photodegradation of 100 mL of aqueous solutions of Rh6G (1×10^{-5} M), obtained as the average of three runs. Values in brackets indicate the k' value used for the determination of the degree of conversion shown in column 5; [g]Conversion achieved by the samples after 20 and 200 min of reaction; [h]Ratio between the average k' values of each of the experiments as compared with the average k' value determined when using 40 mg of the commercial P25 as reference.

at ≈529.8 eV can be assigned to the lattice oxygen in TiO$_2$, while the additional one at 531.7 eV is related to the oxygen in surface hydroxyls (Ti-OH species) and in carboxylic groups.[4,6,29,30] Additional low intensity peaks at ≈532 eV are typically associated to adsorbed water on the titania surface. Analyses in the N2p region could not be carried out due to the presence of adventitious nitrogen in the XPS chamber. In any case, both hybrid materials have similar Ti2p and O1s binding energies than of the L-Tyr-free titanias, which confirms the Ti(IV) and oxygen coordination in our crystalline titanias.
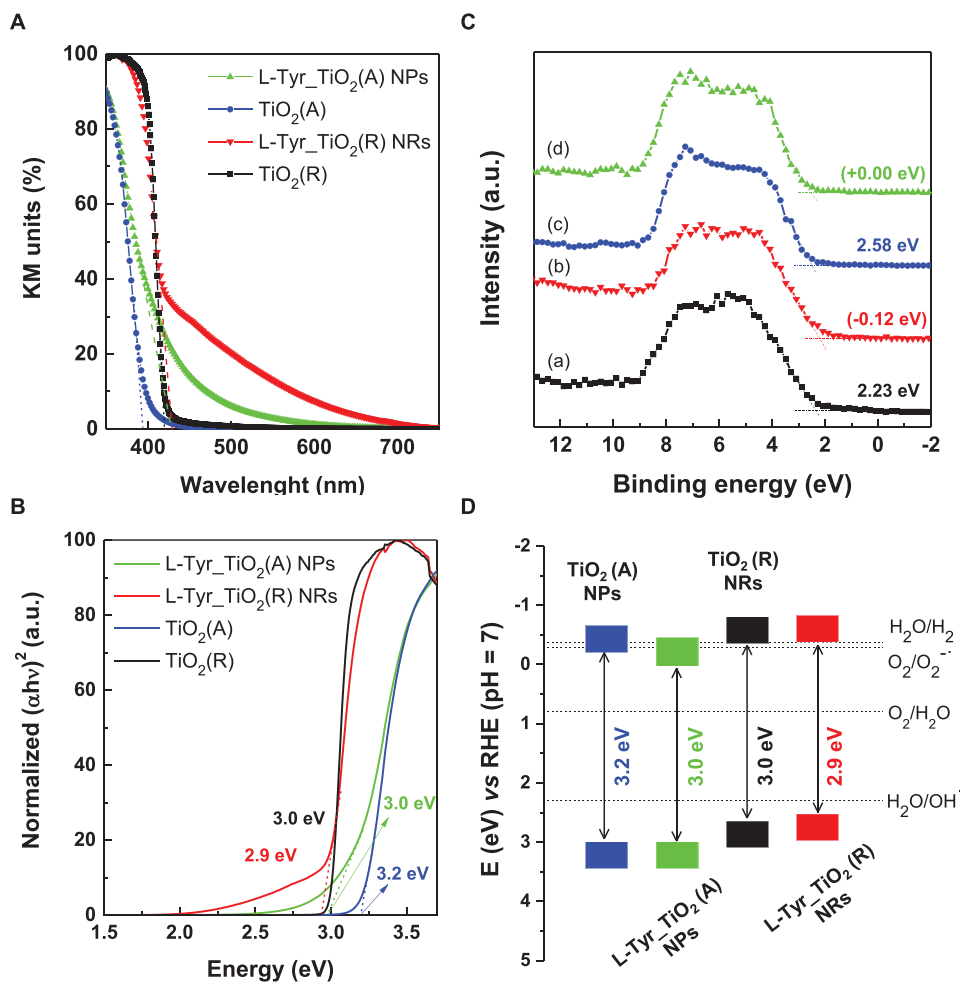
The interparticle mesoporosity of the as-synthesized titanias is significantly affected by their phase composition and morphology—see **Table 1** and **Figure 3**. In detail, both control and hybrid anatase NPs present specific surface areas of ≈200 m^2 g^{-1}, in line with our previously synthesized sol-gel titania-based anatase nanoparticles—Table 1.[3–6] A sharp decrease in both the mesopore volume (up to ≈0.05 cm^3 g^{-1}) and the Brunauer–Emmett–Teller (BET) area (up to ≈20–30 m^2 g^{-1}) is observed in the rutile samples, both control and hybrid. This difference is in line with the lower crystallite size of the former (5 nm versus

≈40 nm), and the much denser structure of the nanorods as compared to the nanoparticles. The surface area of the photocatalysts plays an important role in their photocatalytic activity, as it is related to the accessibility and substrates adsorption on their particle surface,[31,32] as later discussed.

The activation of the photocatalysts in the visible light range is also a critical factor. The optical properties of the as-synthesized materials were assessed by diffuse reflectance UV spectroscopy—**Figure 4**. DRUV spectra show an absorbance edge at 419 nm and 395 nm for control TiO$_2$(R) NRs and TiO$_2$(A) NPs, which corresponds to 2.98 eV and 3.14 eV, respectively, in agreement with the values typically assigned to the band gap of bulk rutile (3.0 eV) and anatase (3.2 eV) structures—Figure 4A (dotted lines indicate the extrapolation of the tangent of that absorption edge to the X–axis cut).[33,34] Red shifts in the DRUV spectra of both the hybrid L-Tyr_TiO$_2$(R) NRs and the L-Tyr_TiO$_2$(A) NPs were observed, the band edge appearing at 430 nm (2.88 eV) and 424 nm (2.92 eV), respectively. Furthermore, additional absorption edges appear at wavelengths higher than 400 nm, associated to intraband gap states.[35]
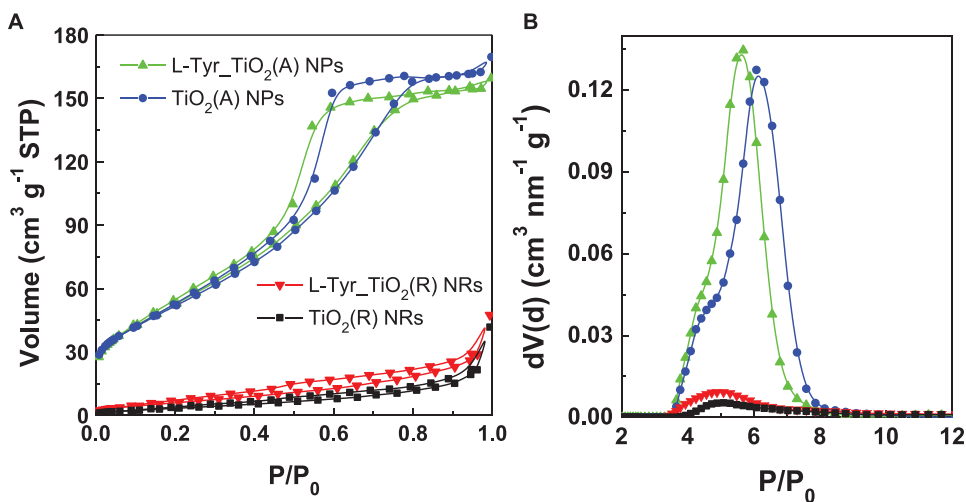
Figure 3. A) N$_2$ adsorption/desorption isotherms at 77 K and B) their corresponding pore sized distribution of suspensions of the hybrid L-Tyr_TiO$_2$(R) NRs and T L-Tyr_TiO$_2$(A) NPs, as compared with the control (L-Tyr-free) titanias.

Adv. Sustainable Syst. **2021**, 5, 2100076

2100076 (5 of 11)

2021 The Authors. Advanced Sustainable Systems published by Wiley-VCH GmbH

Figure 4. A) DRUV spectra, B) estimation of the direct optical band gap from the Tauc plots of the transformed Kubelka–Munk function versus the energy of the light absorbed, C) XPS spectra in the valence band region, and D) DOS scheme of the different synthesized titania-based materials calculated from the direct band gap shown in part (B). The redox potentials at pH = 7 of the main species involved in photocatalytic dye degradations are included.[39,40] Legend in (C) corresponds to: a) TiO_2(R) NRs, b) hybrid L-Tyr_TiO_2(R) NRs, c) TiO_2(A) NPs, and d) L-Tyr_TiO_2(A) NPs.
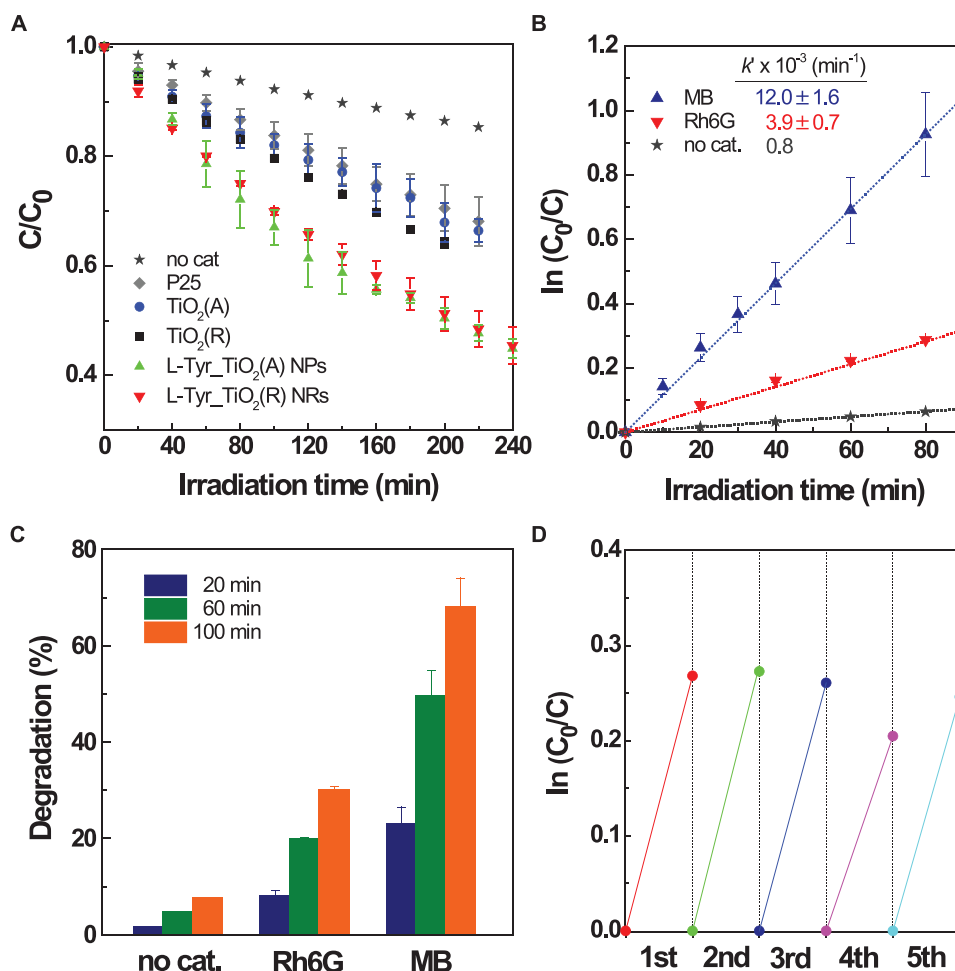
This suggests that i) the optical band gaps of both hybrid L-Tyr_TiO_2(R) NRs and L-Tyr_TiO_2(A) NPs decrease upon the L-Tyr incorporation as compared to the control titanias, and ii) the e⁻—h⁺ pairs are generated in the hybrid materials under long wavelength-visible light irradiation.[36] Optical band gaps were estimated from the Tauc plots of the transformed Kubelka–Munk function considering both direct—Figure 4B— and indirect—Figure S10, Supporting Information—band transitions. Even though anatase is usually considered an indirect band gap semiconductor, and rutile and brookite belong to the direct band gap semiconductor category,[37] we found a better correlation between the band gap values determined by both methods when direct band transitions are considered, even for the anatase materials, as previously reported for anatase nanoparticles—Figure 4B and Table 1.[38]

A comparison between the band edge positions of our materials, after their conversion to the Reversible Hydrogen Electrode (RHE) at pH = 7, is shown in Figure 4C. Albeit the long-standing controversy existing about the position of the valence (VB) and conduction (CB) bands of the different titania polymorphs, their position of the VB and CB bands in our materials is in agreement with that previously described elsewhere[41–45] as well as with our studies on other anatase and rutile titania-based materials.[3–6]

We found a shift to higher binding energies (≈0.36 eV for control materials) in the VB maximum energy of both control and hybrid NRs in comparison to their corresponding NPs, which is consistent with the anatase-to-rutile transition[33,42,45]— Figure 4B,C. In any case, the L-Tyr incorporation during the titania synthesis does not change either the morphology or the size of the obtained products, probably due to the low amount of Tyr incorporated into the titanias. However, it leads to a reduction in its band gap as well as to the presence of intraband gap states associated to the presence of N and O states, which typically activates the visible excitation of titanias, pointing out their potential as photocatalyst under visible light irradiation.

To explore this possibility, the photocatalytic activity of the synthesized materials was evaluated in the degradation reaction of two cationic dyes typically used as model compounds, rhodamine 6G (Rh6G) and methylene blue (MB), under visible light irradiation—see Experimental Section and ESI for details.

**ADVANCED
SCIENCE NEWS**
www.advancedsciencenews.com

**ADVANCED
SUSTAINABLE
SYSTEMS**
www.advsustainsys.com

Figure 5. A) Rh6G photodegradation reaction using as photocatalysts the hybrid L-Tyr_TiO$_2$(R) NRs and hybrid L-Tyr_TiO$_2$(A) NPs, as compared with the L-Tyr-free titania NPs, TiO$_2$(A), and NRs, TiO$_2$(R), and the commercial P25. Photocatalytic activity of the hybrid TiO$_2$(R)-L-Tyr NPs photocatalyst in the degradation reaction of Rh6G and MB: B) plots of ln (C_0/C) as a function of the irradiation time with the corresponding linear fits (dashed lines), and C) degradation at different irradiation times. Inset in (B) shows the apparent constant rate ($k' \times 10^{-3}$, min^{-1}) for each degradation reaction. D) Recycling tests over identical L-Tyr_TiO$_2$(A) NPs samples for degradation of MB. All the experiments were carried out under identical irradiation conditions, using a 400 W medium-pressure mercury lamp (sodium nitrite liquid cut-off filter) as light source, a photocatalyst concentration of 0.4 g L^{-1}, and 1×10^{-5} M aqueous dye solutions.

In the first series of experiments, both hybrids, L-Tyr_TiO$_2$(R) NRs and L-Tyr_TiO$_2$(A) NPs were tested in the photodegradation reaction of Rh6G and compared against their corresponding L-Tyr-free materials, TiO$_2$(A) and TiO$_2$(R), and the commercial P25—Table 1, **Figure 5**A, Figures S11 and S12, Supporting Information. The hybrid materials present a twofold increase in activity as compared to both the control titanias and the commercial P25, achieving decomposition rates of ≈50% after 200 min of irradiation.

Taking into account these results, we chose L-Tyr_TiO$_2$(A) NPs to evaluate the photocatalytic performance of our materials in the degradation of aqueous solutions of another cation dye, that is, MB, under identical irradiation conditions—Figure 5B,C and Figure S13, Supporting Information. Stark differences were found in the degradation of both cationic dyes. The hybrid NPs showed a threefold increase in the MB degradation as compared to the Rh6G, achieving decomposition rates > 70% after only 100 min of irradiation—Figure 5D.

After the degradation reactions, both the Rh6G and the MB solutions were analyzed by HPLC-mass spectrometry (MS). The results were compared to freshly prepared dye solutions—Figures S15 and S16, Supporting Information. The total ion chromatogram (positive mode) and UV chromatogram of the Rh6G solution before irradiation show i) an intense peak at ≈5.0 min, which corresponds to the molecular mass (m/z) of Rh6G after chloride deionization ($m/z = 443$), and ii) two small peaks coming from the deethylation (4.9 min, $m/z = 429.3$) and demethylation (4.6 min, $m/z = 415.2$) of the Rh6G cation—Figure S14A,F, Supporting Information. Similarly, the chromatograms of the initial MB solution show an intense peak at ≈3.8 min, associated to the MB cation ($m/z = 284$), and a low intensity peak at 3.7 min that corresponds to the demethylated MB ($m/z = 270$)—Figure S15B,F, Supporting Information. After the photodegradation, these peaks disappeared, thus suggesting both the MB and Rh6G were degraded (not only bleached) under visible light—Figure S15C–F, Supporting

Adv. Sustainable Syst. **2021**, *5*, 2100076

2100076 (7 of 11)

2021 The Authors. Advanced Sustainable Systems published by Wiley-VCH GmbH

Information.[6,46] MS analysis confirmed the absence of high molar mass fragments typically associated to intermediate MB degradation products.[47–50] In the case of Rh6G, we identified the N-ethyl rhodamine (m/z = 387) by MS, suggesting that the Rh6G degradation occurs via de-ethylation cleavage during the photocatalytic degradation through the initial conversion of the ester group into carboxylic acid giving a possible by-product (m/z = 415), which further degraded by the attack of OH radicals by N-de-ethylation process—Figure S16, Supporting Information. Similar results were reported elsewhere in the photodegradation of Rh6G and RhB.[50] This mechanism is consistent with the shift of the absorption band in the UV–vis absorption spectra of the degradation reaction of Rh6G at different times under visible light irradiation shown in Figure S12E, Supporting Information.[50–52]

Recycling tests were carried out to assess both the reusability and stability of the hybrid NPs as photocatalyst (see ESI for details). Data shown in Figure 5D indicates that the L-Tyr_TiO₂(A) NPs are stable as they can be reused up to five times under the tested conditions. After the five photocatalytic cycles, recovered photocatalysts were characterized by XPS and TEM measurements, and the dye solutions were analyzed by UV–vis spectroscopy. Both the morphology and the XPS spectra in the Ti2p, O2p, and VB regions of L-Tyr_TiO₂(A) NPs remained almost unchanged before and after the MB degradation cycles shown in Figure 5D—Figure S14A, Supporting Information. Moreover, no L-Tyr was detected in the solutions by UV–vis spectroscopy, pointing out the stability of the synthesized L-Tyr_TiO₂ materials—Figure S14B, Supporting Information.

To further confirm both the photocatalytic nature and the stability of the synthesized L-Tyr_TiO₂ materials, three control experiments were carried out (see ESI for details). The first one was the photocatalytic test under dark (non-irradiating) conditions to confirm the photocatalytic nature of the hybrid materials (no dye degradation took place in this case). The second experiment was performed under visible light irradiation, using the same procedure, but without adding the catalyst to the photoreactor system, that is, only with the different dye solutions (see, e.g., sample "no catalyst" in Figure 5A). Under these conditions, we obtained conversions lower than 10%. In the third experiment, we decided to investigate the stability of the as-synthesized hybrids by irradiating a suspension of the hybrid L-Tyr_TiO₂(A) NPs in ultrapure water and in the absence of dyes. As shown in Figure S17, Supporting Information, both the TG and XPS data of the solid remained almost unchanged after the irradiation of the hybrid; and L-Tyr was not detected by UV–vis analysis. These results point out the stability of the hybrid L-Tyr_TiO₂ under the tested conditions.

Based on those results, the following conclusions were drawn. On one hand, the L-Tyr incorporation in titanias by hydrothermal synthesis under acidic conditions allows the synthesis of stable hybrid anatase or rutile titanias with improved photocatalytic activity under visible light. Next, the photocatalytic activities of both hybrid L-Tyr_TiO₂(R) NRs and L-Tyr_TiO₂(A) NPs are very similar, despite their different structure, morphology, and physico-chemical properties. It is generally accepted that anatase has a higher photocatalytic activity than rutile TiO₂. Furthermore, large surfaces areas and high crystallinity are key factors to enhance the reaction of photogenerated

carries with dyes adsorbed on the photocatalyst's surface.[32] Taking into account that there are no major differences in their band gap, the superior photocatalytic activity of both hybrid rutile NRs and anatase NPs is likely due to a synergistic combination between their reduced band gap and additional absorption edges at wavelengths higher than 400 nm, probably associated to intraband gap states due to the N2p and O2p levels of the L-tyrosine.[53] In this sense, the similar efficiency obtained for the anatase NPs and the rutile NRs can be then explained in terms of two main features, the surface area and the crystallinity of both materials. The lower crystallinity of the NPs has a negative impact that counteracts their higher surface area, while the opposite occurs for the NRs (lower surface area but higher crystallinity) yielding to similar photoactivities.

Finally, the photo-degradation rate depends on the cationic dye used as model compound, that is, MB or Rh6G. These results suggest that the dye way seems to play the predominant role, as previously reported for titania-based materials prepared by the in situ incorporation of different organic compounds.[3,4,6] As indicated in the Experimental Section, samples were magnetically stirred in dark before irradiation to achieve adsorption-desorption equilibrium of the dye on the photocatalyst surface. We have observed a higher adsorption of the MB on the titania surface in comparison to the Rh6G, which typically results into the improvement of the photo-degradation rate.

3. Conclusion

In summary, we have successfully synthesized a series of hybrid L-Tyrosine-titanias by a facile method based on the co-condensation of TBOT with the L-Tyrosine during the sol-gel synthesis of the titanias under acidic conditions. The crystalline structure, size, and shape of the as-synthesized hybrid titanias can be easily tuned by varying the pH of the synthesis solution. Anatase nanoparticles of ≈5.3 nm and high surface areas are obtained at pH = 2.2. The increase in the acidity of the medium, however, leads to a dense structure of rutile nanorods roughly bounded. The L-Tyr incorporation into the titania structure does not cause structural changes as compared to the control (L-Tyr-free) titanias. However, this results in a decrease in their band gap as well as in additional absorption edges at wavelengths higher than 400 nm. This combined effect remarkably boosts their photocatalytic efficiency, as compared to the control titanias and the commercial P25, whose mechanism is mainly related to the self-degradation of the cationic dyes, as shown for the degradation of Rh6G and MB under visible light irradiation. Furthermore, the hybrids are stable against both photodegradation and leaching, which points out its potential as photocatalyst for environmental remediation.

4. Experimental Section

Materials: TBOT (97%), L-tyrosine (L-Tyr, FG), hydrochloric acid (HCl, 37%), commercial titania Aeroxide P25 (P25, ≥99.5%), and the Rh6G (99%) were purchased from Aldrich and used without further purification. The FTO coated glass slides (2.2 mm, 13 Ω cm⁻²) were also purchased from Aldrich. Teflon lined stainless steel autoclaves equipped

**ADVANCED
SCIENCE NEWS**

www.advancedsciencenews.com

**ADVANCED
SUSTAINABLE
SYSTEMS**

www.advsustainsys.com

with an outer high-quality stainless steel jacket (homemade) were used as reactors. Both Teflon lined autoclaves and FTO glass substrates were ultrasonicated cleaned before use. For this purpose, they were first cleaned with acetone in an ultrasonication bath for 20 min. Afterward, they were sonicated in a mixture solution of deionized water, acetone, and 2-propanol with volume ratios of 1:1:1 each for 60 min. Finally, the substrates were dried under a nitrogen flow.

Synthesis of Reference Materials: L-Tyr-free titania nanorods, $TiO_2(R)$ NRs, and nanoparticles, $TiO_2(A)$ NPs, were synthesized following the same procedure described above, avoiding the amino acid addition. The synthesis of control nanorods has been adapted from the procedure reported by S. Aydil et al.[22]

Synthesis of the Hybrid Titania-Tyrosine Nanorods, L-Tyr_TiO$_2$(R) NRs: In a typical synthesis, L-Tyr (0.0452 g, 0.25 mmol) was first dissolved in a hydrochloric acid solution prepared by mixing 30 mL of distilled water with 30 mL of hydrochloric acid in the Teflon autoclave. Afterward, the titania precursor, TBOT (2 mL, 5.9 mmol), was added to the above solution and the mixture was magnetically stirred for 10–15 min. The cleaned FTOs (2 substrates) were subsequently placed inside the Teflon lined autoclave, with the conductor facing up, and at an angle of ≈45° against the wall of the autoclave. Finally, hydrothermal synthesis was carried out at 150–170 °C, for different times (0–24 h), under static conditions, in an air oven. The sample-covered FTOs were washed with water, until pH 7, and ethanol successively, and air dried. The solid suspension was also washed with water, until pH 7, and ethanol successively, and then subsequently filtered and dried in an oven at 100 °C for 8 h.

Synthesis of the Hybrid Titania-Tyrosine Nanoparticles, L-Tyr_TiO$_2$(A) NPs: The synthesis of hybrid L-Tyr_$TiO_2(A)$ NPs was adapted from the previously reported procedure for the synthesis of titania-based nanoparticles.[4–6] In a typical synthesis, L-Tyr (0.0452 g, 0.25 mmol) was first dissolved in the titania precursor, TBOT (2 mL, 5.9 mmol) and the mixture was magnetically stirred at 40 °C for 1 h. After cooling the mixture, 31 μL of hydrochloric acid was added to the Teflon autoclave. Afterward, 60 mL of water was added to the above solution and the mixture was magnetically stirred for 100 min. The cleaned FTOs (2 substrates) were subsequently placed inside the Teflon lined autoclave, with the conductor facing up, and at an angle of ≈45° against the wall of the autoclave. Finally, hydrothermal synthesis was carried out at 150 °C for different times (8 and 24 h), under static conditions, in an air oven. The solid suspension was washed with water, until pH 7, and ethanol successively, and then subsequently filtered and dried in an oven at 100 °C for 8 h.

Structures: Structures of TBOT, L-Tyr, and the L-Tyr- TBOT complexes shown in Scheme 1 have been drawn and optimized using ACD/LABS2016.1.1 software, from ACDLabs. Rutile and anatase structures were drawing starting from the CIFs corresponding to each of the structures (mp-2657 and mp-390 respectively).

TG Measurements: The incorporation of L-Tyr into the final materials was evaluated by TG measurements were performed using a Mettler Toledo TG/SDTA analyzer under $O_2:N_2$ (1:4) atmosphere from room temperature to 900 °C at a heating rate of 10 °C min^{-1}.

Powder Diffraction: Synchrotron experiments were performed on the power diffraction station of the BL04-MSPD beamline of the ALBA synchrotron located in the Barcelona area, Spain. Data were collected in transmission mode, at 20 keV, and using the position sensitive detector MYTHEN (beam size, 3 mm horizontal, 0.7 mm vertical). Patterns were recorded in the 0.54–16.0 Å-1 Q-range, at the wavelength $\lambda = 0.6197$ Å, and then x–axis values were further converted to the CuKα radiation for plotting the data. Patterns were registered at room temperature, and with the sample filled in a 1.0-mm-diameter borosilicate capillary. X-ray analysis was carried out as previously reported—see ESI for details.[6]

Morphology: The morphology of the materials was investigated by TEM (solid suspensions) and FESEM (FTO-films). TEM analysis was carried out in a JEOL JEM-1400 Plus instrument. Samples were suspended in ethanol and sonicated for 15 min. A few drops of this suspension were placed on a Lacey Formvar/Carbon copper grid. The ethanol was evaporated at room temperature. The digital analysis of the

TEM micrographs was done using DigitalMicrograph 3.6.1. by Gatan. FESEM analysis of FTO films was carried out in a Merlin VP Compact microscope from Zeiss, at 10 kV. For this purpose, FTO were cut in two parts placed on a SEM stub mount (in both top view and cross-sectional direction), and finally coated with a thin layer of carbon before analysis.

Physisorption Measurements: The porous texture of the materials was characterized by N_2 adsorption/desorption isotherms at 77 K. Measurements were carried out in an AUTOSORB-6 apparatus and the results were analyzed using the software package AUTOSORB1 (Quantachrome Corporation). The samples were previously degassed for 8 h at 100 °C at 5·10^{-5} bars. Pore volume was directly read from the isotherms at a relative pressure of ≈0.95. Specific surface areas were calculated using the BET equation. Interparticle mesopore size was obtained by applying an NLDFT equilibrium model.

XPS: XPS was carried out in a VG-Microtech Multilab instrument, using MgK-alpha radiation of energy 1253.6 eV and pass energy of 50 eV. The analysis pressure during data acquisition was 5×10^{-7} Pa. A careful deconvolution of the spectra was made and the areas under the peaks were estimated by calculating the integral of each peak after subtracting a Shirley background and fitting the experimental peak to a combination of Lorentzian/Gaussian lines of 30–70% proportions. Binding energies were referenced to the C1s line at 284.6 eV from adventitious carbon.[54] XPS spectra of these materials were also obtained in the −10 to 2 eV region to calculate the position of the maximum of their VBs.

Diffuse Reflectance UV Spectroscopy: The band gap of both the organotitanias and the unmodified titania was estimated by DRUV measurements. DRUV spectra were carried out in air, at room temperature, and in the wavelength range 800–200 nm using a Shimadzu UV-2401 PC spectrophotometer with $BaSO_4$ as the reference material. For the estimation of the band-gap, the reflectance data were converted into the equivalent absorption coefficient using the Kubelka-Munk formalism according to Equation (1):

$$F\left(R'\right) = \frac{\left[1 - R'\right]^2}{2R'} \tag{1}$$

where R' is the reflectance value obtained directly from the spectrophotometer. Band gap calculations were based on the $[F(R')h\nu]^{n/2}$ versus photon energy ($h\nu$) plot (Tauc plots).

Both techniques, that is, DRUV and XPS in the VB region, were combined to obtain the density of states (DOS) scheme. Band edge positions were converted to the RHE at pH = 7 by using $E_{RHE} \approx E + 0.059$ pH, where E is the potential corresponding to the maximum VB, as determined by XPS.[55]

Photocatalytic Activity: The photocatalytic activity of synthesized materials was evaluated in the degradation reaction of aqueous solution of two different dyes, Rh6G and MB, using a 400 W Hg medium-pressure lamp as light source. The light output was estimated to be 2.4×10^{16} photons s^{-1}, as determined using ferrioxalate actinometry under operating conditions.[56–58] A freshly prepared $NaNO_2$ solution (2 M, UV cut-off filter > 400 nm) was introduced in the double-walled quartz immersion well, instead of distilled water, for each of the experiments conducted under visible irradiation. In a typical experiment, the photocatalyst (0.4 g L^{-1}) was added to 100 mL of a 1×10^{-5} M dye solution. Before irradiation, samples were magnetically stirred for 60 min in dark to achieve high dispersion and adsorption–desorption equilibrium of the dye on the photocatalyst surface. In all cases, the initial concentration (C_0) has been taken as the concentration after the adsorption–desorption equilibrium was reached. Afterward, the lamp was turned on and the reaction mixture was irradiated with visible light. During the photocatalytic reaction, a known volume of sample was withdrawn every 5–20 min (depending on the system), and the concentration of the Rh6G and MB species was estimated based on the maximum absorbance observed at ≈525 nm and 660 nm, respectively, using a UV–vis spectrometer (V650, Jasco Analytica Spain). After the photocatalytic degradations, the photocatalysts were recovered by centrifugation, washed with distilled water and ethanol, and then characterized by XPS and TEM. Dye solutions before and after

the photocatalytic reactions were analyzed by HPLC-MS and UV–vis spectroscopy. The detailed information can be found in the SI.[6]

Supporting Information

Supporting Information is available from the Wiley Online Library or from the author.

Acknowledgements

Conflict of Interest

The authors declare no conflict of interest.

Data Availability Statement

Research data are not shared.

Keywords

[1] S. Lee, M. Vandiver, B. Viswanathan, V. R. Subramanian, in *Handbook of Climate Change Mitigation*, Vol. 3, Springer, New York **2012**, pp. 1217–1261.

[2] C. Belver, J. Bedia, A. Gómez-Avilés, M. Peñas-Garzón, J. J. Rodriguez, in *Nanoscale Materials in Water Purification*, Elsevier, Amsterdam **2019**, pp. 581–651.

[3] M. Rico-Santacruz, Á. E. Sepúlveda, C. Ezquerro, E. Serrano, E. Lalinde, J. R. Berenguer, J. García-Martínez, *Appl. Catal., B* **2017**, *200*, 93.

[4] M. Rico-Santacruz, Á. E. Sepúlveda, E. Serrano, E. Lalinde, J. R. Berenguer, J. García-Martínez, *J. Mater. Chem. C* **2014**, *2*, 9497.

[5] J. Jiménez-López, N. Linares, E. Serrano, J. García-Martínez, *ChemPlusChem* **2018**, *83*, 390.

[6] G. Sarigul, I. Gómez-Palos, N. Linares, J. García-Martínez, R. D. Costa, E. Serrano, *J. Mater. Chem. C* **2020**, *8*, 12495.

[7] A. Kunzmann, S. Valero, Á. E. Sepúlveda, M. Rico-Santacruz, E. Lalinde, J. R. Berenguer, J. García-Martínez, D. M. Guldi, E. Serrano, R. D. Costa, *Adv. Energy Mater.* **2018**, *8*, 1702583.

[8] Q. D. Truong, T. H. Le, H. T. Hoa, *CrystEngComm* **2017**, *19*, 4519.

[9] U. Schubert, S. Tewinkel, R. Lamber, *Chem. Mater.* **1996**, *8*, 2047.

[10] O. Durupthy, J. Bill, F. Aldinger, *Cryst. Growth Des.* **2007**, *7*, 2696.

[11] O. Durupthy, L. P. H. Jeurgens, J. Bill, *ACS Appl. Mater. Interfaces* **2011**, *3*, 1624.

[12] J. Wang, J. K. Katahara, A. Kumamoto, T. Tohei, A. Sugawara-Narutaki, A. Shimojima, T. Okubo, *RSC Adv.* **2014**, *4*, 9233.

[13] L. Li, Y. Feng, Y. Liu, B. Wei, J. Guo, W. Jiao, Z. Zhang, Q. Zhang, *Appl. Surf. Sci.* **2016**, *363*, 627.

[14] M. Senna, N. Myers, A. Aimable, V. Laporte, C. Pulgarin, O. Baghriche, P. Bowen, *J. Mater. Res.* **2013**, *28*, 354.

[15] V. Jordan, U. Javornik, J. Plavec, A. Podgornik, A. Rečnik, *Sci. Rep.* **2016**, *6*, 1.

[16] M. Gopal, W. J. Moberly Chan, L. C. De Jonghe, *J. Mater. Sci.* **1997**, *32*, 6001.

[17] B. S. Buyuktas, *Transition Met. Chem.* **2006**, *31*, 786.

[18] M. K. Nazeeruddin, S. M. Zakeeruddin, R. Humphry-Baker, M. Jirousek, P. Liska, N. Vlachopoulos, V. Shklover, C. H. Fischer, M. Grätzel, *Inorg. Chem.* **1999**, *38*, 6298.

[19] P. Liu, H. Li, Y. Wang, B. Liu, W. Zhang, Y. Wang, W. Yan, H. Zhang, U. Schubert, *J. Mater. Chem.* **2008**, *18*, 735.

[20] S. F. Shaikh, R. S. Mane, B. K. Min, Y. J. Hwang, O. S. Joo, *Sci. Rep.* **2016**, *6*.

[21] J. G. Li, T. Ishigaki, X. Sun, *J. Phys. Chem. C* **2007**, *111*, 4969.

[22] B. Liu, E. S. Aydil, *J. Am. Chem. Soc.* **2009**, *131*, 3985.

[23] W. Zhou, X. Liu, J. Cui, D. Liu, J. Li, H. Jiang, J. Wang, H. Liu, *CrystEngComm* **2011**, *13*, 4557.

[24] H. Li, X. Duan, G. Liu, X. Jia, X. Liu, *Mater. Lett.* **2008**, *62*, 4035.

[25] C. C. Wang, J. Y. Ying, *Chem. Mater.* **1999**, *11*, 3113.

[26] J. Zhou, B. Song, G. Zhao, G. Han, *Nanoscale Res. Lett.* **2012**, *7*, 217.

[27] A. A. Gribb, J. F. Banfield, *Am. Mineral.* **1997**, *82*, 717.

[28] H. Zhang, J. F. Banfield, *J. Phys. Chem. B* **2000**, *104*, 3481.

[29] L. Zhu, Q. Lu, L. Lv, Y. Wang, Y. Hu, Z. Deng, Z. Lou, Y. Hou, F. Teng, *RSC Adv.* **2017**, *7*, 20084.

[30] W. Hu, Y. Liu, R. L. Withers, T. J. Frankcombe, L. Norén, A. Snashall, M. Kitchin, P. Smith, B. Gong, H. Chen, J. Schiemer, F. Brink, J. Wong-Leung, *Nat. Mater.* **2013**, *12*, 821.

[31] H. Kominami, S. Y. Murakami, J. I. Kato, S. Kera, B. Ohtani, *J. Phys. Chem. B* **2002**, *106*, 10501.

[32] F. Amano, K. Nogami, R. Abe, B. Ohtani, *J. Phys. Chem. C* **2008**, *112*, 9320.

[33] D. O. Scanlon, C. W. Dunnill, J. Buckeridge, S. A. Shevlin, A. J. Logsdail, S. M. Woodley, C. R. A. Catlow, M. J. Powell, R. G. Palgrave, I. P. Parkin, G. W. Watson, T. W. Keal, P. Sherwood, A. Walsh, A. A. Sokol, *Nat. Mater.* **2013**, *12*, 798.

[34] M. Pelaez, N. T. Nolan, S. C. Pillai, M. K. Seery, P. Falaras, A. G. Kontos, P. S. M. Dunlop, J. W. J. Hamilton, J. A. Byrne, K. O'Shea, M. H. Entezari, D. D. Dionysiou, *Appl. Catal., B* **2012**, *125*, 331.

[35] P. Makuła, M. Pacia, W. Macyk, *J. Phys. Chem. Lett.* **2018**, *9*, 6814.

[36] S. Kalathil, M. M. Khan, S. A. Ansari, J. Lee, M. H. Cho, *Nanoscale* **2013**, *5*, 6323.

[37] J. Zhang, P. Zhou, J. Liu, J. Yu, *Phys. Chem. Chem. Phys.* **2014**, *16*, 20382.

[38] M. M. Khan, S. A. Ansari, D. Pradhan, M. O. Ansari, D. H. Han, J. Lee, M. H. Cho, *J. Mater. Chem. A* **2014**, *2*, 637.

[39] X. Li, J. Yu, M. Jaroniec, *Chem. Soc. Rev.* **2016**, *45*, 2603.

[40] X. Li, R. Shen, S. Ma, X. Chen, J. Xie, *Appl. Surf. Sci.* **2018**, *430*, 53.

[41] S. Xie, Q. Zhang, G. Liu, Y. Wang, *Chem. Commun.* **2016**, *52*, 35.

[42] C. Maheu, L. Cardenas, E. Puzenat, C. Geantet, P. Afanasiev, *Phys. Chem. Chem. Phys.* **2018**, *20*, 25629.

[43] Y. Nosaka, A. Y. Nosaka, *J. Phys. Chem. Lett.* **2016**, *7*, 431.

[44] J. Chen, M. Guan, X. Zhang, X. Gong, *RSC Adv.* **2019**, *9*, 36615.

**ADVANCED
SCIENCE NEWS**

www.advancedsciencenews.com

**ADVANCED
SUSTAINABLE
SYSTEMS**

www.advsustainsys.com

[45] A. Di Paola, M. Bellardita, L. Palmisano, F. Parrino, *ECS Trans.* **2019**, *25*, 29.

[46] S. K. Ray, D. Dhakal, Y. K. Kshetri, S. W. Lee, *J. Photochem. Photobiol., A* **2017**, *348*, 18.

[47] Z. He, C. Sun, S. Yang, Y. Ding, H. He, Z. Wang, *J. Hazard. Mater.* **2009**, *162*, 1477.

[48] B. R. V. Ferreira, D. N. Correa, M. N. Eberlin, P. H. Vendramini, *J. Braz. Chem. Soc.* **2017**, *28*, 136.

[49] T. Rasheed, M. Bilal, H. M. N. Iqbal, H. Hu, X. Zhang, *Water, Air, Soil Pollut.* **2017**, *228*, 291.

[50] S. Rajoriya, S. Bargole, V. K. Saharan, *Ultrason. Sonochem.* **2017**, *34*, 183.

[51] T. S. Natarajan, M. Thomas, K. Natarajan, H. C. Bajaj, R. J. Tayade, *Chem. Eng. J.* **2011**, *169*, 126.

[52] P. R. Gogate, P. N. Patil, *Ultrason. Sonochem.* **2015**, *25*, 60.

[53] R. Asahi, T. Morikawa, T. Ohwaki, K. Aoki, Y. Taga, *Science* **2001**, *293*, 269.

[54] C. C. Chusuei, M. A. Brookshier, D. W. Goodman, C. C. Chusuei, M. A. Brookshier, D. W. Goodman, *Langmuir* **1999**, *15*, 2806.

[55] J. Rodríguez-López, A. Minguzzi, A. J. Bard, *J. Phys. Chem. C* **2010**, *114*, 18645.

[56] C. A. Parker, C. G. Hatchard, *J. Phys. Chem.* **1959**, *63*, 22.

[57] C. G. Hatchard, C. A. Parker, *Proc. R. Soc. A* **1956**, *235*, 518.

[58] L. Sun, J. R. Bolton, *J. Phys. Chem.* **1996**, *100*, 4127.

Adv. Sustainable Syst. **2021**, *5*, 2100076

2100076 (11 of 11)

2021 The Authors. Advanced Sustainable Systems published by Wiley-VCH GmbH